Direct sampling method to inverse wave-number-dependent source problems: determination of the support of a stationary source

IOP Publishing Inverse Problems

Inverse Problems **39** (2023) 105008 (23pp) https://doi.org/10.1088/1361-6420/acef51

Direct sampling method to inverse wave-number-dependent source problems: determination of the support of a stationary source

Hongxia Guo, Guanghui Hu and Mengjie Zhao*

School of Mathematical Sciences and LPMC, Nankai University, Tianjin 300071, People's Republic of China

E-mail: 1120200028@mail.nankai.edu.cn

Received 10 December 2022; revised 27 July 2023
Accepted for publication 10 August 2023
Published 1 September 2023

Abstract

This paper is concerned with a direct sampling method for imaging the support of a frequency-dependent source term embedded in a homogeneous and isotropic medium. The source term is given by the Fourier transform of a time-dependent source whose radiating period in the time domain is known. The time-dependent source is supposed to be stationary in the sense that its compact support does not vary along the time variable. Via a multi-frequency direct sampling method, we show that the smallest strip containing the source support and perpendicular to the observation direction can be recovered from far-field patterns at a fixed observation angle. With multiple but discrete observation directions, the shape of the so-called Θ-convex hull of the source support can be recovered. We even extend the proposed algorithm to the case of near-field data in three dimensions. The frequency-domain analysis performed here can be used to handle inverse time-dependent source problems. Our algorithm has low computational overhead and is robust against noise. Numerical experiments in both two and three dimensions have proved our theoretical findings.

Keywords: inverse source problems, frequency-dependent source, multi-frequency data, Fourier transform, direct sampling method

(Some figures may appear in colour only in the online journal)

* Author to whom any correspondence should be addressed.

1. Introduction

1.1. Mathematical formulation

Let $0 \leqslant k_{\min} < k_{\max}$. Consider a frequency-dependent radiating problem in a homogeneous background medium in $\mathbb{R}^d\,(d=2,3)$. The acoustic wave propagation can be governed by the inhomogeneous Helmholtz equation

$$\begin{cases} \Delta u(x,k) + k^2 u(x,k) = f(x,k), & k \in (k_{\min}, k_{\max}),\ x \in \mathbb{R}^d, \\ \lim\limits_{r\to\infty} r^{\frac{d-1}{2}}(\partial_r u - iku) = 0, & r = |x|, \end{cases} \tag{1.1}$$

where $k>0$ is the wavenumber and f is the frequency-dependent source term. The radiation condition at infinity in (1.1) is known as the Sommerfeld radiation condition, which holds uniformly in all directions $\hat{x} = x/|x| \in \mathbb{S}^{d-1} := \{x \in \mathbb{R}^d : |x| = 1\}$. Define $B_R = \{x \in \mathbb{R}^d : |x| < R\}$ for some $R>0$. Throughout the paper we suppose that $f(\cdot,k) \in L^2(B_R)$, $\operatorname{supp} f(\cdot,k) = D \subset B_R$ for all $k \in (k_{\min}, k_{\max})$. Here D is supposed to be a bounded domain such that $\mathbb{R}^d \backslash \overline{D}$ is connected. For every $k>0$, it is well known that there exists a unique solution $u \in H^2(B_R)$ to (1.1) with the explicit representation

$$u(x,k) = \int_D \Phi_d^{(k)}(x,y) f(y,k)\, dy, \qquad x \in \mathbb{R}^d. \tag{1.2}$$

Here, $\Phi_d^{(k)}$ is the fundamental solution to the Helmholtz equation $(\Delta + k^2)u = 0$, given by

$$\Phi_d^{(k)}(x,y) = \begin{cases} \dfrac{i}{4} H_0^{(1)}(k|x-y|), & d=2, \\ \dfrac{e^{ik|x-y|}}{4\pi|x-y|}, & d=3, \end{cases} \qquad x \neq y,\ x,y \in \mathbb{R}^d,$$

and $H_0^{(1)}$ is the Hankel function of the first kind of order zero. The Sommerfeld radiation condition gives rise to the following asymptotic behavior of u at infinity (see [7]):

$$u(x,k) = C_k \frac{e^{ikr}}{r^{\frac{d-1}{2}}} u^\infty(\hat{x},k) + O(r^{-\frac{d+1}{2}}), \qquad r \to \infty, \tag{1.3}$$

where $C_k = e^{i\pi/4}/\sqrt{8\pi k}$ if $d=2$ and $C_k = 1/4\pi$ if $d=3$, and $u^\infty(\cdot,k) \in C^\infty(\mathbb{S}^{d-1})$ is defined as the far-field pattern (or scattering amplitude) of u. It is well known that the function $\hat{x} \mapsto u^\infty(\hat{x},k)$ is real-analytic on $\mathbb{S}^{d-1}$, where $\hat{x} \in \mathbb{S}^{d-1}$ is referred as the observation direction. By (1.2), the far-field pattern u^∞ of u can be expressed as

$$u^\infty(\hat{x},k) = \int_D e^{-ik\hat{x}\cdot y} f(y,k)\, dy, \quad \hat{x} \in \mathbb{S}^{d-1}, \quad k>0. \tag{1.4}$$

In this paper we are interested in the following two inverse problems:

- Extract information on the position and convex-hull (more precisely, the so-called Θ-convex hull (see section 4)) of the support D from knowledge of multi-frequency far-field data at discrete observation directions $\{u^\infty(\hat{x}_j,k) : \hat{x}_j \in \mathbb{S}^{d-1}, k \in (k_{\min}, k_{\max}), j = 1,2,\ldots,J\}$ for some $J \in \mathbb{N}$.
- Determine the position and Θ-convex hull (see section 4) of the support D from knowledge of multi-frequency near-field data at discrete observation points $\{u(x_m,k) : x_m \in \partial B_R, k \in (k_{\min}, k_{\max}), m = 1,2,\ldots,M\}$ for some $M \in \mathbb{N}$, where $\partial B_R = \{x \in \mathbb{R}^3 : |x| = R\}$.

The aim of this paper is to explore a direct sampling method for imaging the support $D = \operatorname{supp} f(\cdot, k)$ from numerical point of view. As done in one of the authors' previous paper [12], the frequency-dependent source term is supposed to be a windowed Fourier transform of some time-dependent source term, i.e. there exists a time window $(t_{\min}, t_{\max}) \subset \mathbb{R}_+$ such that

$$f(x,k) = \int_{t_{\min}}^{t_{\max}} F(x,t) e^{-ikt}\, dt, \quad x \in D,\ k \in (k_{\min}, k_{\max}). \tag{1.5}$$

Here the function $F \in L^\infty(D \times (t_{\min}, t_{\max}))$ satisfies $\operatorname{supp} F(\cdot, t) = D$ for all $t \in (t_{\min}, t_{\max})$ and the time window $(t_{\min}, t_{\max}) \subset \mathbb{R}^+$ is supposed to be available in advance. In this paper F is supposed to be real-valued subject to the positivity condition

$$F(x,t) > 0 \qquad \text{a.e. } x \in D, \quad t \in (t_{\min}, t_{\max}). \tag{1.6}$$

In particular, F is allowed to vanish on the boundary of D for $t \in (t_{\min}, t_{\max})$. It is obvious that the underlying source F is stationary in the sense that the shape of its support does not vary with the time. By the assumption (1.5), we have $f(x,-k) = \overline{f(x,k)}$ for all $k > 0$ and thus $u^\infty(\hat{x}, -k) = \overline{u^\infty(\hat{x}, k)}$.

1.2. Scientific context

If $F(x,t) = f(x)\delta(t)$, it follows from (1.5) that $f(x,k) = f(x)$ is independent of frequencies. In this special case the far-field pattern u^∞ given by (1.3) is nothing else but the Fourier transform of the space-dependent function at the Fourier variable $\xi = k\hat{x} \in \mathbb{R}^d$. For such space-dependent inverse source problems, it is well known that a single frequency data always lead to severely ill-posed problems and uniqueness is impossible due to the existence of non-radiating sources [4, 9]. We refer to [13, 18, 29] for further discussions on recovering polygonal/polyhedral support of a source function with a single pair of data. To overcome the ill-posedness, a wide range of literatures are devoted to frequency-independent inverse problems from multi-frequency far-/near-field data. Uniqueness from the data of an interval of frequencies and observation angles follows straightforwardly, because the these data are analytic with respect to both the wavenumber $k > 0$ and the observation angle. Consequently, a couple of iterative and non-iterative schemes (for example, sampling-type methods) have been proposed for recovering the source function [1, 3, 6, 9, 30] as well as the shape of the support [2, 8, 10, 15, 16, 20, 25]. Concerning sampling-type methods to inverse obstacle scattering problems at a fixed energy and related discussions, we refer the readers to the monographs [7, 17, 26, 27] and the articles [22–24] for an overview. The direct sampling method [5, 14, 19, 21] (which is also called orthogonal sampling method [11, 28]) has also drawn a lot of attentions, because it can be easily implemented and is rather robust against noise. The purpose of this paper is to explore a direct sampling scheme for imaging the support of a class of frequency-dependent source terms in the time-harmonic regime.

When f depends on the wavenumber/frequency, the far-field pattern (1.4) is no longer the Fourier transform of a source function, bringing essential difficulties in proving uniqueness and also in designing inversion schemes. The inverse medium scattering can be equivalently transformed into an inverse wave-number-dependent source problem. To the best of the authors' knowledge, most existing methods cannot be carried over to this case for extracting information on the support and source functions. Although a direct sampling scheme [2] has been tested for recovering the shape of wave-number dependent sources, the numerical examples there were not very satisfactory in comparison with the reconstructions for wave-number independent sources. In [12], a factorization method has been established for recovering source terms of the form (1.5), generalizing the earlier work of [10] to inverse wave-number-dependent source

problems with a known radiating period $[t_{\min}, t_{\max}]$. As mentioned in the previous subsection, such kind of sources arises naturally from the Fourier transform of time-dependent source terms. Motivated by [12] and [2], we consider within this paper the same kind of wave-number-dependent source as [12]. Our approach provides a tool for analyzing inverse time-dependent scattering problems in the frequency domain via Fourier transform.

We compare the factorization scheme of [12] and the direct sampling method proposed in this paper as follows. Fixing an observation direction, one can apply both of them to recover the smallest strip containing the source support and perpendicular to the observation direction from the far-field data in two and three dimensions. Both of them are applicable to the near-field data at multi-frequencies in three dimensions. The factorization method can be implemented with the data from any interval of frequencies, but the direct sampling scheme requires all frequencies in the positive axis. The factorization method was based on a solid analysis from functional analysis, whereas the direct sampling method can be more easily implemented, because the latter only involves inner product calculations. Further, the theoretical justification of the direct sampling, as done in this paper, can be performed under less restrictive mathematical conditions. For example, the positivity condition of the source function F can be further relaxed (see remark 4.1), but the source was required to be coercive in [10, 12].

In this paper the starting time point $t_{\min}$ and the terminal time point $t_{\max}$ of the source radiating period are both supposed to be *a priori* known. If one of them is given, we can also design a direct sampling scheme to recover the Θ-convex hull of the connected support by increasing far-field observation directions. However, it remains unclear to us how to handle the case when neither of them is known. The direct sampling scheme explored within this paper, in particular the inversion theory from a single observation point, can be adapted to extract information on the trajectory of a moving source under additional constraints, which will be reported in our forthcoming papers.

The remaining part of this paper is organized as follows. In the subsequent two sections, we design a direct sampling scheme using multi-frequency far-field patterns at discrete observation direction in $\mathbb{R}^d$. For simplicity, numerical tests will be reported only in $\mathbb{R}^2$ for the far-field case in section 4. In the final section 5, we extend the results of sections 2 and 3 to the case of near-field in three dimensions.

2. Inverse Fourier transform of far-field pattern

Let $\hat{x} \in \mathbb{S}^{d-1}$ be an observation direction and $D \subset \mathbb{R}^d$ be a bounded domain with C^2-smooth boundary. Define

$$\hat{x} \cdot D = \{t \in \mathbb{R} : t = \hat{x} \cdot y \quad \text{for some} \quad y \in D\}.$$

Obviously, $\hat{x} \cdot D$ is an interval of $\mathbb{R}$. Introduce the notations

$$T := t_{\max} - t_{\min}, \quad L_1 := \sup(\hat{x} \cdot D) - \inf(\hat{x} \cdot D), \quad \Lambda_1 := T + L_1. \tag{2.7}$$

In this paper the one-dimensional Fourier and inverse transforms are defined respectively by

$$(\mathcal{F}g)(k) := \int_{\mathbb{R}} g(\xi) e^{-ik\xi}\, d\xi, \quad k \in \mathbb{R},$$
$$(\mathcal{F}^{-1}f)(\xi) := \frac{1}{2\pi} \int_{\mathbb{R}} f(k) e^{ik\xi}\, dk, \quad \xi \in \mathbb{R}.$$

Definition 2.1. The supporting interval of the function $f \in L^2(\mathbb{R})$ is defined as the minimum interval such that f vanishes almost every in the exterior of this interval.

Below we describe the supporting interval of the inverse Fourier transform of the far-field pattern with respect to frequencies at a fixed observation direction.

Lemma 2.1. *Under the assumption (1.6), the supporting interval of* $(\mathcal{F}^{-1}u^\infty(\hat{x},k))(t)$ *is* $H := \big(\inf(\hat{x}\cdot D)+t_{\min},\ \sup(\hat{x}\cdot D)+t_{\max}\big)$ *and the function* $t \longmapsto (\mathcal{F}^{-1}u^\infty)(t)$ *is positive in* H.

Proof. Combining (1.4) and (1.5), the far-field pattern u^∞ of u can be expressed as

$$u^\infty(\hat{x},k) = \int_D f(y,k)e^{-ik\hat{x}\cdot y}dy = \int_{t_{\min}}^{t_{\max}}\int_D F(y,t)e^{-ik(\hat{x}\cdot y+t)}dydt.$$

To write the above expression as a Fourier transform, we observe that

$$\int_D F(y,t)e^{-ik(\hat{x}\cdot y+t)}\,dy = \int_{\mathbb{R}} e^{-ik\xi}\left(\int_{\Gamma(\xi-t)} F(y,t)ds(y)\right)d\xi$$

where $\Gamma(t)\subset D$ is defined as

$$\Gamma(t) := \{y\in D : \hat{x}\cdot y = t\},\quad t\in\mathbb{R}.$$

Note that when $\Gamma(\xi-t)=\emptyset$, the aforementioned integral over $\Gamma(\xi-t)$ is taken as zero. Consequently,

$$u^\infty(\hat{x},k) = \int_{\mathbb{R}} e^{-ik\xi}g(\xi)d\xi = (\mathcal{F}g)(k), \tag{2.8}$$

with

$$g(\xi) := \int_{t_{\min}}^{t_{\max}}\int_{\Gamma(\xi-t)} F(y,t)ds(y)dt = \int_{\xi-t_{\max}}^{\xi-t_{\min}}\int_{\Gamma(t)} F(y,\xi-t)ds(y)dt. \tag{2.9}$$

Since $\Gamma(t)=\emptyset$ for $t<\inf(\hat{x}\cdot D)$ and $t>\sup(\hat{x}\cdot D)$, it is obvious that

$$g(\xi)=0 \qquad \text{if} \quad \xi<\inf(\hat{x}\cdot D)+t_{\min} \quad \text{or} \quad \xi>\sup(\hat{x}\cdot D)+t_{\max}.$$

It remains to prove

$$g(\xi)>0 \qquad \text{if} \quad \xi\in\big(\inf(\hat{x}\cdot D)+t_{\min},\ \sup(\hat{x}\cdot D)+t_{\max}\big). \tag{2.10}$$

For such ξ, we suppose that

$$\xi = \inf(\hat{x}\cdot D)+t_{\min}+\epsilon \quad \text{for some} \quad \epsilon\in(0,\Lambda_1). \tag{2.11}$$

Then it holds that

$$\xi - t\in(t_{\min},t_{\min}+\epsilon), \quad \text{if} \quad t\in\big(\inf(\hat{x}\cdot D),\ \inf(\hat{x}\cdot D)+\epsilon\big).$$

Now we rewrite g as

$$g(\xi) = \int_{\inf(\hat{x}\cdot D)}^{\inf(\hat{x}\cdot D)+\varepsilon}\int_{\Gamma(t)} F(y,\xi-t)ds(y)dt.$$

Observing for any $\epsilon\in(0,\Lambda_1)$ that

$$\big(\inf(\hat{x}\cdot D),\ \inf(\hat{x}\cdot D)+\epsilon\big)\cap\big(\inf(\hat{x}\cdot D),\sup(\hat{x}\cdot D)\big)\neq\emptyset,$$
$$\big(t_{\min},t_{\min}+\epsilon\big)\cap\big(t_{\min},t_{\max}\big)\neq\emptyset,$$

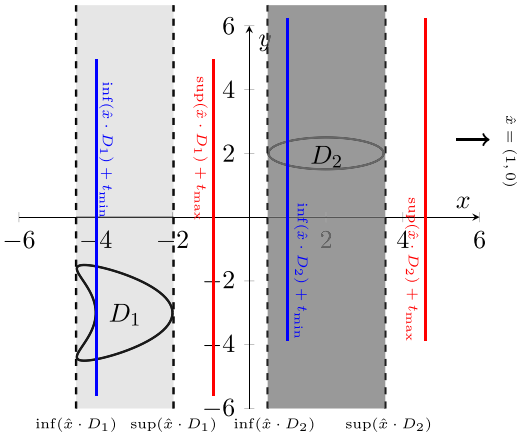

Figure 1. Examples of D_1 and D_2 satisfying the assumption (A). Here $t_{\min} = 0.5$, $t_{\max} = 1$, D_1 is kite-shaped, D_2 is elliptical and $\hat{x} = (1,0)$.

we deduce from the positivity assumption of F that g must be positive in $\big(\inf(\hat{x}\cdot D)+t_{\min},\ \sup(\hat{x}\cdot D)+t_{\max}\big)$. □

In lemma 2.2 below, we assume that $D = D_1 \cup D_2 \subset \mathbb{R}^d$ consists of two disconnected components D_1 and D_2. We make the following assumption on the distance between D_1 and D_2:

Assumption (A): It holds that

$$\sup(\hat{x}\cdot D_1)+t_{\max} < \inf(\hat{x}\cdot D_2)+t_{\min} \quad \text{or} \quad \sup(\hat{x}\cdot D_2)+t_{\max} < \inf(\hat{x}\cdot D_1)+t_{\min}.$$

In other words, $\inf(\hat{x}\cdot D_2) - \sup(\hat{x}\cdot D_1) > T$ or $\inf(\hat{x}\cdot D_1) - \sup(\hat{x}\cdot D_2) > T$.

Physically, the assumption (A) means that the wave signals radiated from D_1 and D_2 can be separated in the observation direction $\hat{x}$: see figures 1 and 2. Otherwise, the support of the these waves can be overlapped along the propagating direction $\hat{x}$.

Lemma 2.2. *The supporting interval of* $(\mathcal{F}^{-1}u^\infty(\hat{x},k))(t)$ *is* $H_1 \cup H_2$ *where* $H_j = \big(\inf(\hat{x}\cdot D_j)+t_{\min},\ \sup(\hat{x}\cdot D_j)+t_{\max}\big)$ *and the function* $t \longmapsto (\mathcal{F}^{-1}u^\infty)(t)$ *is positive in* $H_1 \cup H_2$. *Further,* $H_1 \cup H_2$ *is a subset of* $H = \big(\inf(\hat{x}\cdot D)+t_{\min},\ \sup(\hat{x}\cdot D)+t_{\max}\big)$ *under the assumption (A), and* $H_1 \cup H_2 = H$ *if the assumption (A) does not hold.*

Remark 2.1. The assumption (A) ensures that the intervals H_1 and H_2 have no intersections, i.e. $H_1 \cap H_2 = \emptyset$. In particular, $(\hat{x}\cdot D_1) \cap (\hat{x}\cdot D_2) = \emptyset$.

Proof. As done in the proof of lemma 2.1, the far-field takes the form

$$\begin{aligned} u^\infty(\hat{x},k) &= \int_{t_{\min}}^{t_{\max}} \int_{D_1\cup D_2} F(y,t) e^{-ik(\hat{x}\cdot y+t)} dy dt \\ &= \int_{\mathbb{R}} e^{-ik\xi} g(\xi) d\xi = (\mathcal{F}g)(k). \end{aligned} \tag{2.12}$$

Here $g = g_1 + g_2$ with the functions g_j $(j = 1,2)$ defined as

$$g_j(\xi) := \int_{t_{\min}}^{t_{\max}} \int_{\Gamma_j(\xi-t)} F(y,t) ds(y) dt = \int_{\xi-t_{\max}}^{\xi-t_{\min}} \int_{\Gamma_j(t)} F(y,\xi-t) ds(y) dt. \tag{2.13}$$

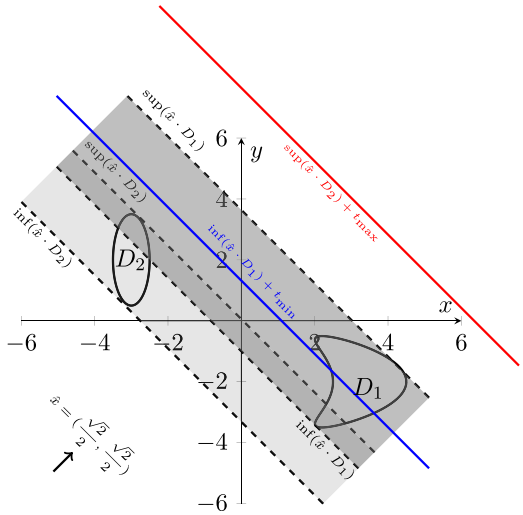

Figure 2. Examples of D_1 and D_2 which do not satisfy the assumption (A). Here $t_{\min} = 1$, $t_{\max} = 5$ and $\hat{x} = (\sqrt{2}/2, \sqrt{2}/2)$. The acoustic waves radiated from D_1 and D_2 can be overlapped.

The set $\Gamma_j(t) \subset D_j$ is defined as

$$\Gamma_j(t) := \{y \in D_j : \hat{x}\cdot y = t\}, \quad t \in \mathbb{R}.$$

Hence, the inverse Fourier transform of the multi-frequency far-field patterns (2.12) is $\mathcal{F}^{-1}u^\infty = g = g_1 + g_2$. It follows from lemma 2.1 that $\mathrm{supp}(g_j) = H_j$ and $g_j > 0$ in H_j for $j = 1,2$. This proves $\mathrm{supp}(\mathcal{F}^{-1}u^\infty) = \mathrm{supp}(g) = H_1 \cup H_2$ and g is positive in $H_1 \cup H_2$.

Noting that $H_1 \cap H_2 = \emptyset$ under the assumption (A), we obtain that $H_1 \cup H_2$ is a subset of H. If $H_1 \cap H_2 \neq \emptyset$, it is obvious that $H_1 \cup H_2 = H$.

□

3. Indicator and test functions

From lemmas 2.1 and 2.2, one can extract information on the interval $\big(\inf(\hat{x}\cdot D) + t_{\min}, \sup(\hat{x}\cdot D) + t_{\max}\big)$ by taking the inverse Fourier transform of $u^\infty(\hat{x},k)$ for all $k > 0$. Since $t_{\min}$ and $t_{\max}$ are both given, this obviously yields information on the strip $\hat{x}\cdot D$. In this section we shall design proper indicator functions to image the support $\hat{x}\cdot D$ in a more straightforward manner.

We first suppose that D is connected. Given an observation direction $\hat{x}$, we want to design an indicator function $y \longmapsto I(y)$, $y \in \mathbb{R}^d$ such that

$$I(y) = \begin{cases} 0 & \text{if} \quad \hat{x}\cdot y \notin \hat{x}\cdot D, \\ \text{finite positive number} & \text{if otherwise.} \end{cases}$$

Introduce two test functions

$$\phi_1^{(\hat{x})}(y,k) := e^{-ik(\hat{x}\cdot y + t_{\min})}, \quad \phi_2^{(\hat{x})}(y,k) := e^{-ik(\hat{x}\cdot y + t_{\max})},$$

and two auxiliary indicator functions

$$I_j^{(\hat{x})}(y) = \int_{\mathbb{R}} u^\infty(\hat{x},k)\,\overline{\phi_j^{(\hat{x})}(y,k)}\,dk, \quad j = 1,2, \tag{3.14}$$

where $y \in \mathbb{R}^d$ is referred to as the sampling variable. Below we characterize the support of $I_j^{(\hat{x})}$ $(j = 1, 2)$.

Theorem 3.1. *Let $\hat{x} \in \mathbb{S}^{d-1}$ be fixed. We have*

$$I_1^{(\hat{x})}(y) = \begin{cases} 0 & \text{for} \quad \hat{x}\cdot y \notin \big(\inf(\hat{x}\cdot D), \sup(\hat{x}\cdot D) + T\big), \\ \text{finite positive number} & \text{for} \quad \hat{x}\cdot y \in \big(\inf(\hat{x}\cdot D), \sup(\hat{x}\cdot D) + T\big); \end{cases} \tag{3.15}$$

$$I_2^{(\hat{x})}(y) = \begin{cases} 0 & \text{for} \quad \hat{x}\cdot y \notin \big(\inf(\hat{x}\cdot D) - T, \sup(\hat{x}\cdot D)\big), \\ \text{finite positive number} & \text{for} \quad \hat{x}\cdot y \in \big(\inf(\hat{x}\cdot D) - T, \sup(\hat{x}\cdot D)\big). \end{cases} \tag{3.16}$$

Proof. Denote by $\delta(\cdot)$ the Dirac delta function. The test functions $\phi_j^{(\hat{x})}(y,k)$ $(j = 1, 2)$ can be rephrased as

$$\begin{aligned} \phi_1^{(\hat{x})}(y,k) &= \int_{\mathbb{R}} e^{-ik\xi}\delta(\xi - \hat{x}\cdot y - t_{\min})d\xi = [\mathcal{F}(\delta(\xi - \hat{x}\cdot y - t_{\min}))](k), \\ \phi_2^{(\hat{x})}(y,k) &= \int_{\mathbb{R}} e^{-ik\xi}\delta(\xi - \hat{x}\cdot y - t_{\max})d\xi = [\mathcal{F}(\delta(\xi - \hat{x}\cdot y - t_{\max}))](k). \end{aligned} \tag{3.17}$$

Applying the Parseval's identity and properties of Fourier transform, we deduce from (2.8) and (3.14) that

$$\begin{aligned} I_1^{(\hat{x})}(y) &= \int_{\mathbb{R}} u^{\infty}(\hat{x},k)\overline{\phi_1^{(\hat{x})}(k)}dk \\ &= \int_{\mathbb{R}} [\mathcal{F}g(\xi)](k)\ \overline{[\mathcal{F}(\delta(\xi - \hat{x}\cdot y - t_{\min}))](k)}dk \\ &= \int_{\mathbb{R}} g(\xi)\ \delta(\xi - \hat{x}\cdot y - t_{\min})d\xi \\ &= g(\hat{x}\cdot y + t_{\min}) \end{aligned} \tag{3.18}$$

where g is defined by (2.9). From lemma 2.1, we know $\operatorname{supp} g = \big(\inf(\hat{x}\cdot D) + t_{\min},\ \sup(\hat{x}\cdot D) + t_{\max}\big)$ and g is positive in $\operatorname{supp} g$. Therefore, $g(\hat{x}\cdot y + t_{\min}) > 0$ for all $y \in \mathbb{R}^d$ such that $\hat{x}\cdot y \in \big(\inf(\hat{x}\cdot D), \sup(\hat{x}\cdot D) + T\big)$. On the other hand, it is also obvious that $g(\hat{x}\cdot y + t_{\min}) = 0$ for all $\hat{x}\cdot y \notin \big(\inf(\hat{x}\cdot D), \sup(\hat{x}\cdot D) + T\big)$, which proves (3.15). The results in (3.16) can be verified analogously. □

The indicator function for imaging $\hat{x}\cdot D$ is defined as follows:

$$I^{(\hat{x})}(y) := \left[\frac{1}{I_1^{(\hat{x})}(y)} + \frac{1}{I_2^{(\hat{x})}(y)}\right]^{-1} = \frac{I_1^{(\hat{x})}(y)\, I_2^{(\hat{x})}(y)}{I_1^{(\hat{x})}(y) + I_2^{(\hat{x})}(y)}.$$

Now we state the indicating behavior of $I^{(\hat{x})}$.

Theorem 3.2. *Let $\hat{x} \in \mathbb{S}^{d-1}$ be fixed and assume that D is connected. Then*

$$I^{(\hat{x})}(y) = \begin{cases} 0 & \text{for} \quad \hat{x}\cdot y \notin \hat{x}\cdot D, \\ \text{finite positive number} & \text{for} \quad \hat{x}\cdot y \in \hat{x}\cdot D. \end{cases} \tag{3.19}$$

Proof. It is obvious that

$$\hat{x}\cdot D = \big(\inf(\hat{x}\cdot D) - T, \sup(\hat{x}\cdot D)\big) \cap \big(\inf(\hat{x}\cdot D), \sup(\hat{x}\cdot D) + T\big).$$

Hence, if $\hat{x}\cdot y \in \hat{x}\cdot D$, one deduces from theorem 3.1 that $0 < I_j^{(\hat{x})}(y) < \infty$ for $j = 1, 2$, implying $0 < I^{(\hat{x})}(y) < \infty$.

On the other hand, if $\hat{x}\cdot y \notin \hat{x}\cdot D$, we have either $\hat{x}\cdot y \notin \big(\inf(\hat{x}\cdot D)-T, \sup(\hat{x}\cdot D)\big)$ or $\hat{x}\cdot y \notin \big(\inf(\hat{x}\cdot D), \sup(\hat{x}\cdot D)+T\big)$. In the former case, we get $I_1^{(\hat{x})}(y)=0$ and in the latter case $I_2^{(\hat{x})}(y)=0$. Hence, there must hold $I^{(\hat{x})}(y)=0$ for $\hat{x}\cdot y \notin \hat{x}\cdot D$.

□

If D consists of two components, we can get analogous results to theorem 3.2. In the following theorem, the intervals H_1 and H_2 corresponding to D_1 and D_2 are defined as in lemma 2.2.

Theorem 3.3. *Let $D = D_1 \cup D_2$ where $D_j \subset \mathbb{R}^d$ are bounded domains such that $D_1 \cap D_2 = \emptyset$ and let $\hat{x} \in \mathbb{S}^{d-1}$ be fixed. Under the assumption (A), we have*

$$I^{(\hat{x})}(y) = \begin{cases} 0 & \text{for} \quad \hat{x}\cdot y \notin \bigcup_{j=1,2}\{\hat{x}\cdot D_j\}, \\ \text{finite positive number} & \text{for} \quad \hat{x}\cdot y \in \bigcup_{j=1,2}\{\hat{x}\cdot D_j\}. \end{cases} \tag{3.20}$$

If the assumption (A) does not hold, then $I^{(\hat{x})}(y)=0$ for $\hat{x}\cdot y \notin \hat{x}\cdot D$.

Proof. Let g_1 and g_2 be defined as in (2.13) with the support $\mathrm{supp}(g_j) = H_j$ for $j=1,2$. Analogously to the proof of theorem 3.2, we obtain

$$\begin{aligned} I_1^{(\hat{x})}(y) &= g_1(\hat{x}\cdot y + t_{\min}) + g_2(\hat{x}\cdot y + t_{\min}), \\ I_2^{(\hat{x})}(y) &= g_1(\hat{x}\cdot y + t_{\max}) + g_2(\hat{x}\cdot y + t_{\max}). \end{aligned}$$

Under the assumption (A), it follows from lemma 2.2 that $\mathrm{supp}(g_1+g_2) = H_1 \cup H_2$ and $g_1 + g_2$ is positive in $H_1 \cup H_2$. Hence,

$$\begin{aligned} I_1^{(\hat{x})}(y) = 0 \quad \text{if} \quad \hat{x}\cdot y \notin \bigcup_{j=1,2} \big(\inf(\hat{x}\cdot D_j),\ \sup(\hat{x}\cdot D_j)+T\big), \\ 0 < I_1^{(\hat{x})}(y) < \infty \quad \text{if} \quad \hat{x}\cdot y \in \bigcup_{j=1,2} \big(\inf(\hat{x}\cdot D_j),\ \sup(\hat{x}\cdot D_j)+T\big), \\ I_2^{(\hat{x})}(y) = 0 \quad \text{if} \quad \hat{x}\cdot y \notin \bigcup_{j=1,2} \big(\inf(\hat{x}\cdot D_j)-T,\ \sup(\hat{x}\cdot D_j)\big), \\ 0 < I_1^{(\hat{x})}(y) < \infty \quad \text{if} \quad \hat{x}\cdot y \in \bigcup_{j=1,2} \big(\inf(\hat{x}\cdot D_j)-T,\ \sup(\hat{x}\cdot D_j)\big). \end{aligned}$$

By the definition of $I^{(\hat{x})}$, one can get the relations shown in (3.20) under the assumption (A). Without the assumption (A), we deduce from the proof of theorem 3.2 that

$$\begin{aligned} \mathrm{supp}\left(I_1^{(\hat{x})}\right) &\subset \big(\inf(\hat{x}\cdot D),\ \sup(\hat{x}\cdot D)+T\big), \\ \mathrm{supp}\left(I_2^{(\hat{x})}\right) &\subset \big(\inf(\hat{x}\cdot D)-T,\ \sup(\hat{x}\cdot D)\big) \end{aligned}$$

and $I_j^{(\hat{x})} > 0$ in $\mathrm{supp}(I_1^{(\hat{x})})$ for $j=1,2$. This yields

$$\mathrm{supp}(I^{(\hat{x})}) = \mathrm{supp}(I_1^{(\hat{x})}) \cap \mathrm{supp}(I_2^{(\hat{x})}) = \big(\inf(\hat{x}\cdot D),\ \sup(\hat{x}\cdot D)\big) = \hat{x}\cdot D.$$

In other words, $I^{(\hat{x})}(y)=0$ for $\hat{x}\cdot y \notin \hat{x}\cdot D$. □

4. Two-dimensional (2D) numerical tests with multi-frequency far-field patterns

In this section, we shall numerically reconstruct the source support $D \subset \mathbb{R}^2$ from the multi-frequency far-field data $\{u^\infty(\hat{x}_m,k) : \hat{x}_m \in \mathbb{S}^{d-1}, k \in (0,K), m = 1,2,\ldots,M\}$, where $K>0$ is a truncated number of wave-number k. Unless otherwise stated, we suppose that D is connected. Since the function $k \mapsto u^\infty(\hat{x},k)$ can be analytically extended onto the negative axis by $u^\infty(\hat{x},-k) = \overline{u^\infty(\hat{x},k)}$ for $k>0$, the indicators functions (3.14) can be approximated by

$$\begin{aligned} I_j^{(\hat{x})}(y) &\approx \int_{-K}^{K} u^\infty(\hat{x},k)\ \overline{\phi_j^{(\hat{x})}(y,k)}\ dk \\ &= \int_0^K u^\infty(\hat{x},k)\ \overline{\phi_j^{(\hat{x})}(y,k)}\ dk + \int_{-K}^0 u^\infty(\hat{x},k)\ \overline{\phi_j^{(\hat{x})}(y,k)}\ dk \\ &= \int_0^K u^\infty(\hat{x},k)\ \overline{\phi_j^{(\hat{x})}(y,k)}\ dk + \int_0^K \overline{u^\infty(\hat{x},k)}\ \phi_j^{(\hat{x})}(y,k)\ dk \\ &= 2\mathrm{Re}\left\{\int_0^K u^\infty(\hat{x},k)\ \overline{\phi_j^{(\hat{x})}(y,k)}\ dk\right\} \end{aligned} \tag{4.21}$$

for $j=1,2$. Using multiple observations, we shall utilize the reciprocal of the sum of $(I^{(\hat{x}_m)})^{-1}$ $(m=1,2,\ldots,M)$ as a new indicator, that is,

$$I(y) = \left[\sum_{m=1}^{M} \frac{1}{I^{(\hat{x}_m)}(y)}\right]^{-1} = \left[\sum_{m=1}^{M} \frac{I_1^{(\hat{x}_m)}(y) + I_2^{(\hat{x}_m)}(y)}{I_1^{(\hat{x}_m)}(y)\ I_2^{(\hat{x}_m)}(y)}\right]^{-1}. \tag{4.22}$$

The convex hull of the source region D (that is, the intersections of all half spaces containing D) can be approximated by the intersection of the strips $\mathcal{S}^{(\hat{x}_m)} := \{y \in \mathbb{R}^2 : \hat{x}\cdot y \in \hat{x}_m \cdot D\}$. Define the Θ-convex hull of D (see [29]) determined by the directions $\{\hat{x}_m : m = 1,2,\ldots,M\}$ as

$$\Theta_D := \bigcap_{m=1}^{M} \mathcal{S}^{(\hat{x}_m)}.$$

Since $\Theta_D \subset \mathcal{S}^{(\hat{x}_m)}$ for all $m=1,2,\ldots,M$, one can reconstruct the Θ-convex hull of D from discrete observation directions by plotting the indicator function $I(y)$.

Theorem 4.1. *Let $D \subset \mathbb{R}^2$ be connected. We have*

$$I(y) = \begin{cases} 0 & \text{for} \quad y \notin \Theta_D, \\ \text{finite positive number} & \text{for} \quad y \in \Theta_D. \end{cases} \tag{4.23}$$

Proof. If $y \in \Theta_D$, then $y \in \mathcal{S}^{(\hat{x}_m)}$ for all $m=1,2,\ldots,M$, yielding that $\hat{x}_m \cdot y \in \hat{x}_m \cdot D$. Hence, one deduces from theorem 3.1 that $0 < I^{(\hat{x}_m)}(y) < \infty$ for all $m=1,2,\ldots,M$, implying $0 < I(y) < \infty$. On the other hand, if $y \notin \Theta_D$, it holds that $y \notin \mathcal{S}^{(\hat{x}_\ell)}$ for some $\hat{x}_\ell$. Again using theorem 3.1 we obtain $\frac{1}{I^{(\hat{x}_\ell)}(y)} = \infty$. Hence, there must hold $I(y) = 0$ for $y \in \Theta_D$. □

To balance the indicator values for different observation directions, we normalize the indicator functions I and $I^{(\hat{x}_m)}$ by

$$\tilde{I}^{(\hat{x}_m)}(y) := \frac{I^{(\hat{x}_m)}(y) - \min_{y\in\Omega} I^{(\hat{x}_m)}(y)}{\max_{y\in\Omega} I^{(\hat{x}_m)}(y) - \min_{y\in\Omega} I^{(\hat{x}_m)}(y)}$$

$$I(y) = \left[\sum_{m=1}^{M} \frac{1}{\tilde{I}^{(\hat{x}_m)}(y)}\right]^{-1}, \quad \tilde{I}(y) := \frac{I(y) - \min_{y\in\Omega} I(y)}{\max_{y\in\Omega} I(y) - \min_{y\in\Omega} I(y)}$$

where $\Omega \supset D$ is a search domain for imaging D. The normalization ensures that the values of the indicators $\tilde{I}^{(\hat{x}_m)}$ and $\tilde{I}$ are positive with the maximum value one. By theorem 3.2, one can expect that $\tilde{I}$ should be relatively larger in D than those values in the exterior of D. Our numerical examples are tested by the normalized indicators.

With all observations $\hat{x} \in \mathbb{S}^{d-1}$, one can easily obtain the following uniqueness result.

Theorem 4.2. *Suppose that the positivity condition (1.6) holds on the connected domain $D \subset \mathbb{R}^d$ and the radiating period $(t_{\min}, t_{\max})$ is given. Then the multi-frequency far-field patterns $\{u^\infty(\hat{x},k) : \forall\, \hat{x} \in \mathbb{S}^{d-1}, k \in (0,K)\}$ with some $K > 0$ uniquely determine the convex hull of D.*

Note that the knowledge of $u^\infty(\hat{x},k)$ in the frequency interval $(0,K)$ is equivalent to the far-field data for all $k > 0$, due to the analyticity of $u^\infty(\hat{x},k)$ in $k > 0$.

Remark 4.1. We think that the positivity condition over D can be further relaxed, for example, F remains positive only in a neighborhood of $\partial(D \times (t_{\min}, t_{\max}))$. Even without the positivity assumption, one can get the same uniqueness if the source function F and the boundary of the domain D are both analytic.

Remark 4.2. In the direct sampling scheme, it is essential to explain properties of the indicator function $I^{(\hat{x})}$ at a fixed observation point. In this paper the indicating behavior of the truncated indicator (4.21) is interpreted as the approximation of the original indicators (3.14) whose properties are rigorously justified in theorem 3.1. This is different from an alternative explanation made in [2] where the truncated indicator was shown to decay as $1/|y|$ when the sampling variable y moves away from D.

In the subsequent two subsections, we will report numerical examples using far-field data in two dimensions.

4.1. Reconstructions from a single observation direction

In this subsection, we illustrate numerical reconstructions of the strip $\mathcal{S}^{(\hat{x})}$ from the multi-frequency far-field data $\{u^\infty(\hat{x},k) : k \in (0,K]\}$ using the indicator $\tilde{I}^{(\hat{x})}$ with one single observation direction. It is supposed that $\hat{x} = (\cos\theta,\ \sin\theta)$ with some fixed $\theta \in (0, 2\pi]$. In order to discretize the wave-number interval $(0,K]$, we take

$$k_n := n\Delta k \quad \text{with} \quad \Delta k := \frac{K}{N} > 0, \quad n = 1, \ldots, N.$$

Hence, the discretization of the multi-frequency far-field data can be $\{u^\infty(\hat{x},k_n) : k_n = n\Delta k, n = 1,2,\ldots,N\}$. We select the source functions that are real-valued and are constrained by (1.6). If not otherwise stated, we choose $K = 20$ and $N = 200$ as the default setting. In figures 3(a)–(c), we set $F(x,t) = 1$ supported on a kite-shaped domain, fix $\theta = \pi/2$ and plot the normalized indicators $\tilde{I}_j^{(\hat{x})}$ for $j = 1,2$ and $\tilde{I}^{(\hat{x})}$. To make inversion results more intuitive, we set a threshold $\varepsilon > 0$ in figures 3(d)–(f), respectively. It is obvious that $\tilde{I}_j^{(\hat{x})}$ $(j = 1,2)$ can be used to capture the strip $\hat{x} \cdot D$ with a shift $T = 2$ on the upper and bottom boundaries. The strip $\mathcal{S}^{(\hat{x})}$ has been accurately recovered by the normalized indicator $\tilde{I}^{(\hat{x})}$.

Three different source functions and three observation directions are selected in figure 4. We choose $F(x,t) = 1$ and $\theta = \pi/4$ in figure 4(a); $F(x,t) = t$ and $\theta = 3\pi/4$ in figure 4(b) and $F(x,t) = (x_1^2 + x_2^2 + 10)t$ and $\theta = 2\pi$ in figure 4. These figures are reconstructed by the normalized indicator $\tilde{I}^{(\hat{x})}$ and are not processed by a threshold. One can conclude that strip $\mathcal{S}^{(\hat{x})}$ can be well recovered by using the multi-frequency data at a single observation direction.

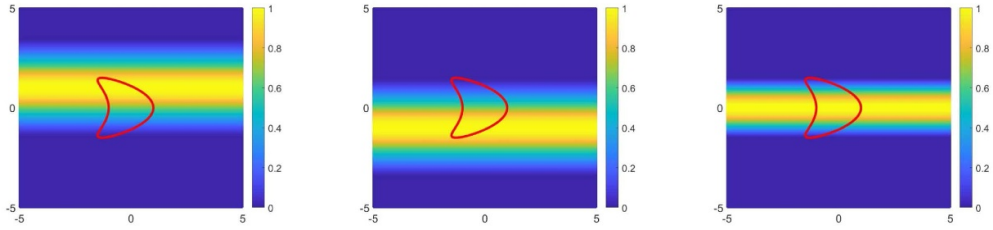

(a) Indicator $\tilde{I}_1^{(\hat{x})}$ (b) Indicator $\tilde{I}_2^{(\hat{x})}$ (c) Indicator $\tilde{I}^{(\hat{x})}$

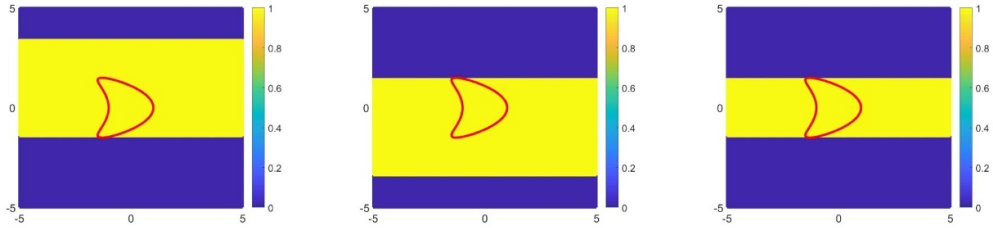

(d) $\tilde{I}_1^{(\hat{x})}$, $\varepsilon = 0.007$ (e) $\tilde{I}_2^{(\hat{x})}$, $\varepsilon = 0.007$ (f) $\tilde{I}^{(\hat{x})}$, $\varepsilon = 0.007$

Figure 3. Reconstructions of a kite-shaped support with different indicators defined as (3.15), (3.16) and (3.19). The Fourier transform window is $(t_{\min}, t_{\max}) = (0, 2)$.

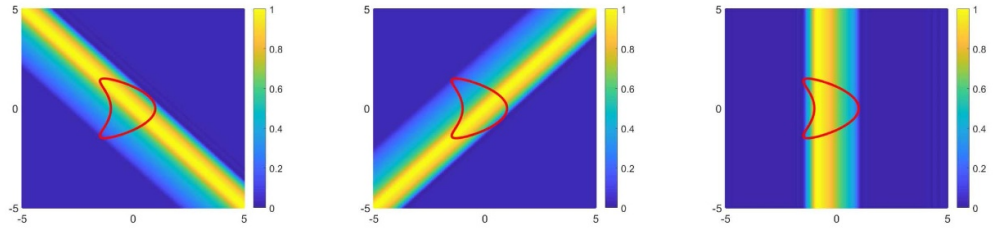

(a) $F = 1, \theta = \pi/4$ (b) $F = t, \theta = 3\pi/4$ (c) $F = (x_1^2 + x_2^2)t, \theta = 2\pi$

Figure 4. Reconstructions for a kite-shaped support by using a single observation direction $\hat{x} = (\cos\theta, \sin\theta)$ and multi-frequency far-field data. The Fourier transform window is $(0, 0.1)$.

Next, we perform numerical tests by using different Fourier transform windows $(t_{\min}, t_{\max})$. We fix $\hat{x} = (\cos\theta, \sin\theta)$, $\theta = 3\pi/4$ and fix the source function $F(x,t) = (x_1^2 + x_2^2 + 10)t$ supported on the kite-shaped domain. We set $t_{\min} = 0$ in figure 5. Take $t_{\max} = 1$, $N = 200$ in figure 5(a); $t_{\max} = 3$, $N = 300$ in figure 5(b); $t_{\max} = 8$, $N = 800$ in figure 5(c). It is obvious that the source support lies in the smallest strip perpendicular to the observation direction. Fixing $T = t_{\max} - t_{\min} = 0.1$, we change $t_{\min} = 1, 2, 3$ in figure 6. The two group numerical results have shown that the choice of the Fourier transform window $(t_{\min}, t_{\max})$ does not effect the reconstructions at a single observation direction.

Finally, we consider a support with two disconnected components, a kite and an ellipse, which satisfy the assumption (A) for some observation direction $\hat{x}$. In figure 7(a), the observation angle is taken as $\theta = \pi/4$, and the strip goes along the direction of $3\pi/4$, separating the

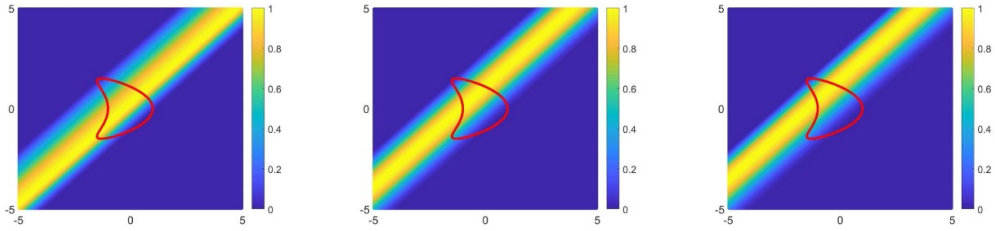

(a) $T = 1$ (b) $T = 3$ (c) $T = 8$

Figure 5. Reconstructions of a kite-shaped support with $F(x,t) = (x_1^2 + x_2^2 + 10)t$ and $\theta = 3\pi/4$ with different Fourier transform windows $(t_{\min}, t_{\max}) = (0, T)$.

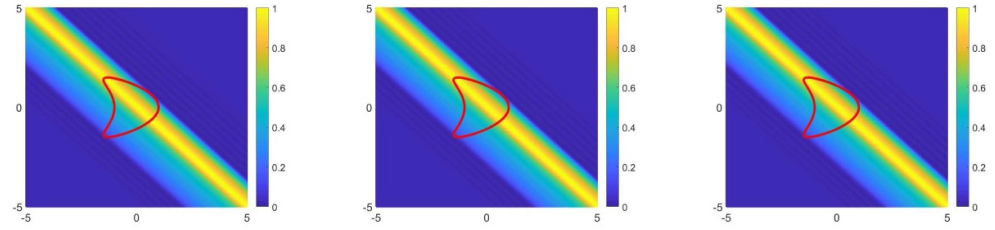

(a) $t_{\min} = 1,\ T = 0.1$ (b) $t_{\min} = 2,\ T = 0.1$ (c) $t_{\min} = 3,\ T = 0.1$

Figure 6. Reconstructions of a kite-shaped support with $F(x,t) = (x_1^2 + x_2^2 + 10)t$ and $\theta = \pi/4$ withdifferent Fourier transform windows $(t_{\min}, t_{\min} + T)$.

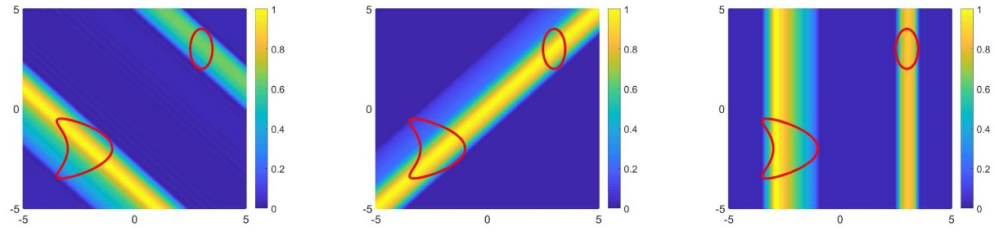

(a) $\theta = \pi/4$ (b) $\theta = 3\pi/4$ (c) $\theta = 2\pi$

Figure 7. Reconstructions of a kite-ellipse-shaped support from different observation angles. Here $F(x,t) = (x_1^2 + x_2^2 + 10)t$ and the Fourier transform window is taken as $(0, 0.1)$.

two supports precisely. The kite-ellipse-shaped supports lie within the strips obtained from the observation angle $3\pi/4$, which are visualized in figure 7(b). Since the distance assumption(A) is not satisfied at the angle $\theta = 3\pi/4$, the two supports are not separated but lie within the strip perpendicular to the observation direction. We set the observation angle to $\theta = 2\pi$ in figure 7(c). The recovered strips along the direction $(1, 0)$ precisely separates the two components.

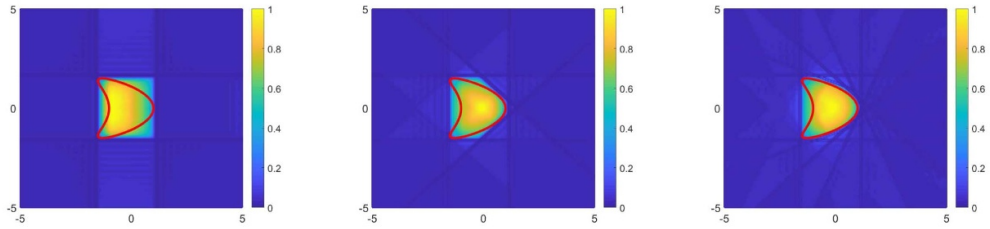

(a) $M = 2$ (b) $M = 4$ (c) $M = 8$

Figure 8. Reconstructions of two disconnected supports with the source function $F(x,t) = (x_1^2 + x_2^2 + 10)t$, the Fourier transform window $(0, 0.1)$ and using M directions.

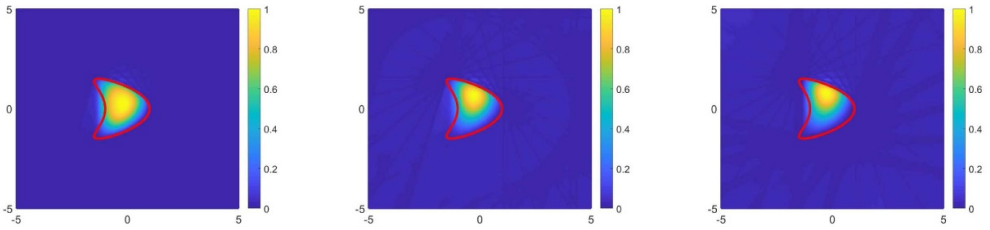

(a) $T = 1$ (b) $T = 3$ (c) $T = 5$

Figure 9. Reconstructions of a kite-shaped support source $F(x,t) = (x_1^2 + x_2^2 + 10)t$ with different Fourier transform windows $(0, T)$ by using $M = 12$ observations.

4.2. Reconstructions from discrete observation directions

In this subsection, we test the performance of the multi-frequency sampling method with M observation directions $\hat{x}_m = (\cos\theta_m,\ \sin\theta_m)$, $\theta_m = \dfrac{m-1}{M}\pi$, $m = 1, 2, \ldots, M$. The numerical results for reconstructing the location and Θ-convex-hull of the kite-shaped source support are shown in figure 8, where $F(x,t) = (x_1^2 + x_2^2 + 10)t$. Evidently, the recovery quality has been improved as the number of observation angles increases in figure 8. In the case $M = 8$, the shape of the kite can be well restored.

As done in the single observation case, we also illustrate the reconstructions with different radiating periods $(0, T)$ of the Fourier transformation in figure 9. Fixing $t_{\min} = 0$ and $K = 20$, we set $T = t_{\max} - t_{\min} = 1$ and $N = 200$ in figure 9(a); $T = 3$ and $N = 200$ in figure 9(b); $T = 5$ and $N = 300$ in figure 9(c). Even for large T we observe that the reconstructed Θ-convex hull reflects the location and shape of the support.

In figure 10, we focus on the case of two disconnected supports. The kite-ellipse-shaped domain can be restored pretty well by using 16 observations. We set the source function $F(x,t) = (x_1 + 10)t$ supported on the kite centered at $(0, -2)$ and the ellipse centered at $(0, 3)$ in figure 10(a); $F(x,t) = (x_1^2 + x_2^2 + 10)t$ supported on the kite centered at $(-2, -2)$ and the ellipse centered at $(3, 3)$ in figure 10(b); $F(x,t) = (x_2 + 10)t$ with the kite-center at $(-2, 0)$ and the ellipse center at $(3, 0)$ in figure 10(c). These figures are truncated by a threshold $\varepsilon = 0.30$ in figures 10(d)–(f).

We show the numerical examples in figure 11 by using different Fourier transform windows $(0, T)$. The reconstructions of two disconnected supports are displayed in figure 11, where we

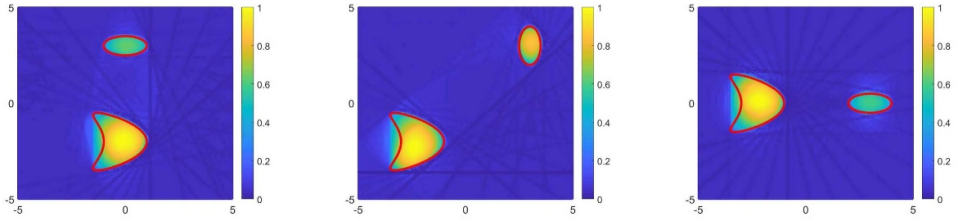

(a) $F = (x_1 + 10)t$ (b) $F = (x_1^2 + x_2^2 + 10)t$ (c) $F = (x_2 + 10)t$

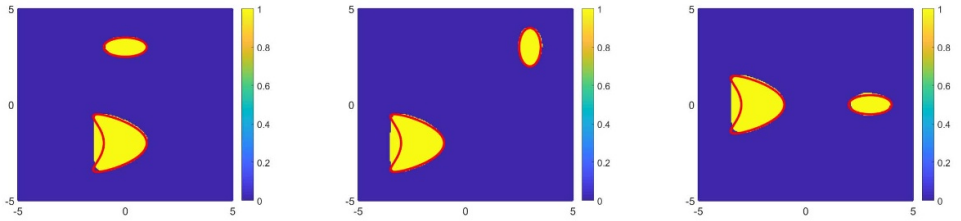

(d) $F = (x_1 + 10)t$, $\varepsilon = 0.30$ (e) $F = (x_1^2 + x_2^2 + 10)t$, $\varepsilon = 0.30$ (f) $F = (x_2 + 10)t$, $\varepsilon = 0.30$

Figure 10. Reconstructions of a kite-ellipse-shaped support with different locations and sources by using 16 observations. The Fourier transform windows is $(0, 0.1)$.

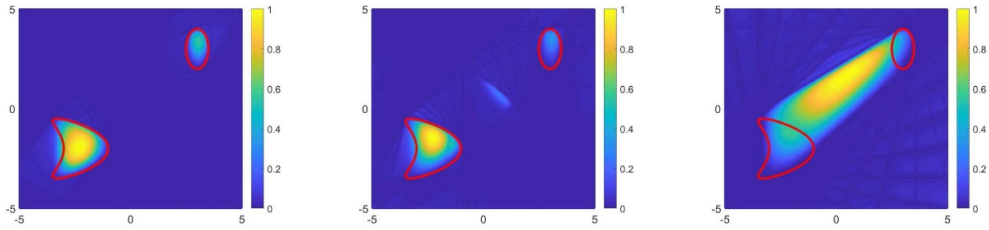

(a) $T = 1$ (b) $T = 3$ (c) $T = 7$

Figure 11. Reconstructions of a kite-shaped support with $F(x,t) = (x_1^2 + x_2^2 + 10)t$ with different Fourier transform windows $(0, T)$.

fix $t_{\min} = 0$ and $K = 20$. We choose $T = t_{\max} - t_{\min} = 1$ and $N = 200$ in figure 11(a), $T = 3$ and $N = 300$ in figure 11(b), $T = 7$ and $N = 300$ in figure 11(c). In the last case of $T = 7$, the reconstruction is distorted because the assumption (A) is not satisfied. Here we choose $M = 16$ observation directions.

Finally, we examine the sensitivity of the direct sampling algorithm to noise. The synthetic data is polluted by noise via the following formula

$$u_\delta^\infty(\hat{x}, k) = u^\infty(\hat{x}, k) + \delta \mathbf{R} \circ u^\infty(\hat{x}, k), \tag{4.24}$$

where δ is the noise level, $\mathbf{R} \in \mathbb{R}^{W \times N}$ is a uniformly distributed random matrix with the random variable ranging from -1 to 1 and $\circ$ represents the Hadamard product. We test three different noise levels $\delta = 10\%$, 50%, and 100%. The recovered results are displayed in figure 12, from

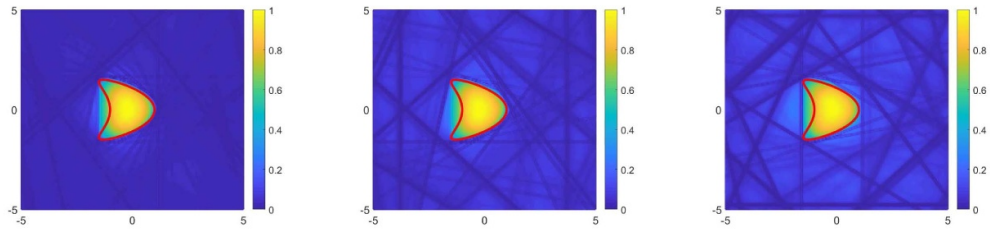

(a) $\delta = 10\%$ (b) $\delta = 50\%$ (c) $\delta = 100\%$

Figure 12. Reconstructions of a kite-shaped support with $F(x,t) = (x_1^2 + x_2^2 + 10)t$ with different noise levels δ.

which one can conclude that the inversion algorithm is rather robust against noise. This phenomenon has also been reported in other existing literatures (see e.g. [5, 19]). In our tests, we find that boundaries of the strips $\mathcal{S}^{(\hat{x}_m)}$ are also visible at high noise levels.

5. Reconstructions from near-field data in $\mathbb{R}^3$

In this section, we suppose that $D \subset B_R \subset \mathbb{R}^3$ for some $R > 0$ and take the near-field data on discrete observation points lying on $|x| = R$. We remark that it seems difficult to extend the results of this section to two dimensions, perhaps due to the lack of Huygens' principle in 2D. For simplicity we supposed that D is connected. For source supports with multiple components, one can proceed with analogous arguments to the far-field case.

5.1. Indicator and test functions

By (1.2), the near-field data can be expressed as

$$u(x,k) = \int_D \frac{e^{ik|x-y|}}{4\pi\,|x-y|} \int_{t_{\min}}^{t_{\max}} F(y,t)e^{-ikt}dtdy, \quad x \in \mathbb{R}^3.$$

The supporting interval of the Fourier transform of the near-field data with respect to frequencies is stated below.

Lemma 5.1. *Let the assumption (1.6) hold true and fix some $x_0 \in \partial B_R$. The supporting interval of $\mathcal{F}^{-1}[u(x_0,k)]$ is*

$$H_0 := \left(t_{\min} - \sup_{z\in D} |x_0 - z|,\ t_{\max} - \inf_{z\in D} |x_0 - z| \right).$$

Moreover, the function $t \longmapsto (\mathcal{F}^{-1}u)(t)$ is positive in H_0.

Proof. For $t \in \mathbb{R}$, define

$$\Gamma(t) := \{y \in D : |x_0 - y| = t\}.$$

Like the far-field case, we reformulate the near-field expression as the Fourier transform by

$$\begin{aligned} u(x_0,k) &= \int_{t_{\min}}^{t_{\max}} \int_D F(y,t) \frac{e^{-ik(t-|x_0-y|)}}{4\pi|x_0-y|} dydt \\ &= \int_{t_{\min}}^{t_{\max}} \int_{\mathbb{R}} \int_{\Gamma(t-\xi)} F(y,t) \frac{e^{-ik\xi}}{4\pi(t-\xi)} ds(y) d\xi\, dt \\ &= \int_{\mathbb{R}} e^{-ik\xi} h(\xi) d\xi = (\mathcal{F}h)(k), \end{aligned} \tag{5.25}$$

where

$$h(\xi) := \int_{t_{\min}-\xi}^{t_{\max}-\xi} \int_{\Gamma(t)} \frac{F(y,t+\xi)}{4\pi t} ds(y) dt, \quad \xi \in \mathbb{R}. \tag{5.26}$$

Since $\Gamma(t) = \emptyset$ for $t < \inf_{z\in D} |x_0 - z|$ or $t > \sup_{z\in D} |x_0 - z|$, we have $h(\xi) = 0$ for $\xi < t_{\min} - \sup_{z\in D} |x_0 - z|$ or $\xi > t_{\max} - \inf_{z\in D} |x_0 - z|$. Thus,

$$\operatorname{supp}(\mathcal{F}^{-1} u(x_0,k)) = \operatorname{supp}(h) \subset H_0.$$

Next we show that h is positive for $t \in H_0$. For $\xi \in H_0$, we suppose that

$$\xi = t_{\min} - \sup_{z\in D} |x - z| + \varepsilon \quad \text{for some} \quad \varepsilon \in (0, \Lambda_2),$$

with the notations

$$\Lambda_2 := T + L_2, \quad L_2 := \sup_{z\in D} |x_0 - z| - \inf_{z\in D} |x_0 - z|.$$

The number $\Lambda_2 > 0$ represents the length of the interval H_0. By the assumption (1.6), we deduce from (5.26) that

$$h(\xi) = \int_{\inf_{z\in D} |x_0-z|}^{\sup_{z\in D} |x_0-z| - \varepsilon + T} \int_{\Gamma(t)} \frac{F(y,t+\xi)}{4\pi t} ds(y) dt. \tag{5.27}$$

We observe that

$$\xi + t \in \big(t_{\min} - L_2 + \varepsilon, t_{\max}\big) \qquad \text{if} \quad t \in \big(\inf_{z\in D} |x_0 - z|), \sup_{z\in D} |x_0 - z| - \varepsilon + T\big),$$

and that for any $\epsilon \in (0, \Lambda_2)$,

$$\begin{aligned} \big(\inf_{z\in D} |x_0 - z|), \sup_{z\in D} |x_0 - z| - \varepsilon + T\big) \cap \big(\inf_{z\in D} |x_0 - z|), \sup_{z\in D} |x_0 - z|\big) \neq \emptyset, \\ \big(t_{\min} - L + \varepsilon, t_{\max}\big) \cap \big(t_{\min}, t_{\max}\big) \neq \emptyset. \end{aligned}$$

This together with the positivity of F proves $h > 0$ in H_0.

□

For some fixed $|x| = R$, we introduce two test functions

$$\psi_1^{(x)}(y,k) := e^{ik(|x-y| - t_{\min})}, \quad \psi_2^{(x)}(y,k) := e^{ik(|x-y| - t_{\max})},$$

and two auxiliary indicator functions

$$I_j^{(x)}(y) := \int_{\mathbb{R}} u(x,k)\,\overline{\psi_j^{(x)}(y,k)}\,dk, \quad j=1,2. \tag{5.28}$$

From the multi-frequency near-field data $u(x,k)$ at the observation point $x \in \partial B_R$, we want to image the annular domain

$$\mathcal{A}^{(x)} := \left\{ y \in \mathbb{R}^3 : \inf_{z\in D} |x-z| < |x-y| < \sup_{z\in D} |x-z| \right\}.$$

For this purpose, we design the indicator function

$$I^{(x)}(y) := \left[\frac{1}{I_1^{(x)}(y)} + \frac{1}{I_2^{(x)}(y)} \right]^{-1} = \frac{I_1^{(x)}(y)\, I_2^{(x)}(y)}{I_1^{(x)}(y) + I_2^{(x)}(y)}, \quad y \in \mathbb{R}^3. \tag{5.29}$$

Theorem 5.1. *Let $D \subset B_R$ for some $R>0$ and we fix some $|x|=R$. Then it holds that*

$$I^{(x)}(y) = \begin{cases} 0 & \text{for} \quad y \notin \mathcal{A}^{(x)}, \\ \text{finite positive number} & \text{for} \quad y \in \mathcal{A}^{(x)}. \end{cases}$$

Proof. Arguing analogously to the proof of (3.17), we see

$$\psi_1^{(x)}(y,k) = [\mathcal{F}(\delta(\xi + |x-y| - t_{\min})](k),$$
$$\psi_2^{(x)}(y,k) = [\mathcal{F}(\delta(\xi + |x-y| - t_{\max})](k).$$

In view of (5.25) and (5.26), we get

$$I_1^{(x)}(y) = h(t_{\min} - |x-y|), \quad I_2^{(x)}(y) = h(t_{\max} - |x-y|). \tag{5.30}$$

Hence, using the results of lemma 5.1 yields

$$I_1^{(x)}(y) = \begin{cases} 0 & \text{for} \quad |x-y| \notin \left(\inf_{z\in D}|x-z| - T, \sup_{z\in D}|x-z|\right), \\ \text{finite positive number} & \text{for} \quad |x-y| \in \left(\inf_{z\in D}|x-z| - T, \sup_{z\in D}|x-z|\right); \end{cases}$$
$$I_2^{(x)}(y) = \begin{cases} 0 & \text{for} \quad |x-y| \notin \left(\inf_{z\in D}|x-z|, \sup_{z\in D}|x-z| + T\right), \\ \text{finite positive number} & \text{for} \quad |x-y| \in \left(\inf_{z\in D}|x-z|, \sup_{z\in D}|x-z| + T\right). \end{cases}$$

Now, the indicating behavior of $I^{(x)}$ follows from the fact $\operatorname{supp} I^{(x)} := \operatorname{supp} I_1^{(x)} \cap \operatorname{supp} I_2^{(x)} = (\inf_{z\in D}|x-z|, \sup_{z\in D}|x-z|)$.

□

Using the multi-frequency data taking at discrete observation points $x_m \in \partial B_R$ ($m = 1,2,\ldots,M$), one can design a new indicator function via superposition for imaging the intersection $\bigcap_{m=1}^{M} \mathcal{A}^{(x_m)}$. We omit the details for brevity, since it can be done analogously to the far-field case.

5.2. *Numerical tests using near-field data in* $\mathbb{R}^3$

In this section, we present numerical reconstructions of the source support $D \subset \mathbb{R}^3$ from the multi-frequency data $\{u(x_m,k) : x_m \in \partial B_R, k \in (0,K), m = 1,2,\ldots,M\}$ at discrete observation points. Here $K>0$ is a truncated number. In view of theorem 5.1, the smallest annular domain containing the support and centered at x can be restored using the indicator $I^{(x)}$ (5.29) from the near-field data $u(x,k)$, $k \in (0,K)$. To discretize the wave-number interval, we take

$$k_n := n\Delta k \ \text{ with } \ \Delta k := \frac{K}{N} > 0.$$

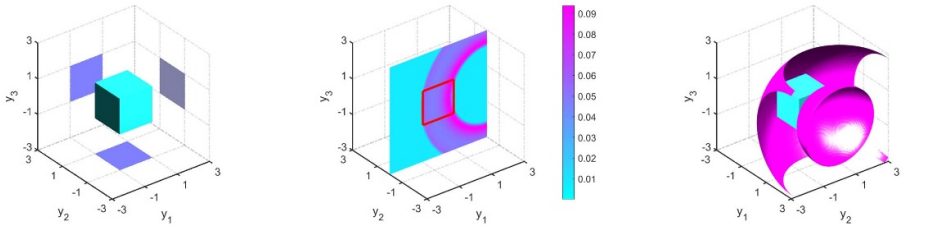

(a) Geometry of source support (b) Slice at $y_2 = 0$ (c) Iso-surface level $= 1.8 \times 10^{-2}$

Figure 13. Reconstruction of a cube-shaped support using multi-frequency data from a single observation point.

The indicator functions $I_j^{(x)}(y)$ defined by (5.28) can be approximated by

$$I_j^{(x)}(y) \sim \left| 2\mathrm{Re}\left\{ \int_0^K u(x,k)\overline{\psi_j^{(x)}(y,k)}\, dk \right\} \right|, \ j = 1,2.$$

Then the source support D can be imaged by plotting the indicator

$$I(y) = \left[\sum_{m=1}^{M} \frac{1}{I^{(x_m)}(y)} \right]^{-1} = \left[\sum_{m=1}^{M} \frac{I_1^{(x_m)}(y) + I_2^{(x_m)}(y)}{I_1^{(x_m)}(y)\, I_2^{(x_m)}(y)} \right]^{-1}, \quad y \in \mathbb{R}^3. \tag{5.31}$$

Similarly to the far-field case (see theorem 4.1), we have the following result with discrete observation points.

Theorem 5.2. *Suppose that the positivity condition (1.6) holds on the domain $D \subset B_R$. Then it holds that*

$$I(y) = \begin{cases} 0 & \text{for} \quad y \notin \bigcap_{m=1}^{M} \mathcal{A}^{(x_m)}, \\ \text{finite positive number} & \text{for} \quad y \in \bigcap_{m=1}^{M} \mathcal{A}^{(x_m)}. \end{cases} \tag{5.32}$$

Unless otherwise stated, we take $K = 20$ and $N = 100$ as default in the following numerical examples.

Example 1. In this example, we illustrate the reconstructions of the annular $\mathcal{A}^{(x)}$ for a cube by plotting the indicator $I^{(x)}(y)$ in (5.29). We set the time dependent source function to be $F(x,t) = (x_1^2 + x_2^2 + x_3^2 + 1)(t+1)$ which satisfies the positivity condition (1.6). We assume that F is supported in $D \times (t_{\min}, t_{\max})$ with $t_{\min} = 0$ and $t_{\max} = 0.1$. The cube D is defined by (see figure 13(a))

$$D = \{(x_1, x_2, x_3) : |x_1| < 1, |x_2| < 1 \text{ and } |x_3| < 1\}.$$

We take the observation point at $x = (3,0,0)$ and plot the indicator in the search domain $[-3,3]^3$. Figures 13(b) and (c) show visualizations of the indicator function (5.29) in the search area. Figure 13(b) shows a slice of the reconstruction at $y_2 = 0$. We see that the cross of the plane $y_2 = 0$ with the smallest annular containing the square (in red) and centered at $x = (3,0,0)$ is nicely reconstructed. Figure 13(c) illustrates an iso-surface of the reconstruction at the iso-level 1.8×10^{-2}. The iso-surfaces perfectly enclose the cube-shaped support.

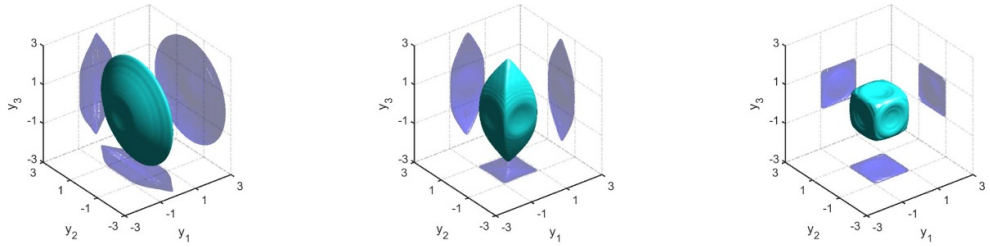

(a) $M = 2$ (b) $M = 4$ (c) $M = 6$

Figure 14. Reconstruction of a cube-shaped support using multi-frequency data from multiple observation points. The number of observation points is $M = 2$, 4, 6 and the corresponding iso-surface levels are 2.5×10^{-2}, 1.2×10^{-2} and 7×10^{-3}, respectively.

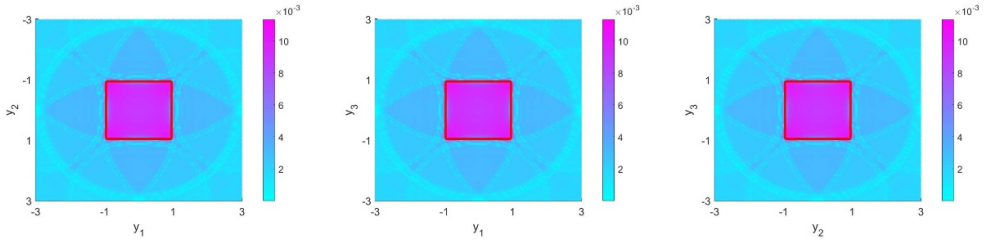

(a) Slice at $y_3 = 0$ (b) Slice at $y_2 = 0$ (c) Slice at $y_1 = 0$

Figure 15. Slices of the reconstruction from six observation points at the planes $y_3 = 0$, $y_2 = 0$ and $y_1 = 0$.

Example 2. We continue example 1 with multiple observation points. A visualization of the indicator function (5.31) is shown in figure 14 with M observation points. The multi-frequency data at two observation points $\{(3,0,0),(-3,0,0)\}$ are utilized in figure 14(a), and the data at four observation points $\{(3,0,0),(-3,0,0),(0,3,0),(0,-3,0)\}$ in figure 14(b), where the position of the source is nicely reconstructed. Using six observation points $\{(3,0,0),(-3,0,0),(0,3,0),(0,-3,0),(0,0,3),(0,0,-3)\}$ in figure 14(c), we can see that both the location and Θ-convex-hull of the source support are well reconstructed.

To clearly illustrate the reconstructions in figure 14, we also plot the projections of the images onto the oy_1y_2, oy_1y_3 and oy_2y_3 planes. From these 2D visualizations one sees that the projections at y_1-axis are $[-1,1]$ in figure 14(a), the projections on $0y_1y_2$ is square $[-1,1]^2$ in figure 14(b) and the projections are all squares $[-1,1]^2$ in figure 14(c), which prove the accuracy of the three-dimensional reconstructions. Figure 15 shows slices of the reconstruction at the planes $y_1 = 0$, $y_2 = 0$ and $y_3 = 0$ using the data at six observation points (see figure 14(c)). For comparison we also demonstrate the boundary of the source support's slice with the red solid line. These slices also confirm the accuracy of our algorithm.

In figures 16 and 17, we show slices of the reconstructions of a cubic source with a longer radiating period $(t_{\min}, t_{\max})$. Different Fourier transform windows from the data observed at six observation points (like the case in figure 14(c)) are used. The radiating period (resp. Fourier transform window) is taken as $(0, 0.5)$ in figure 16 and $(0, 1)$ in figure 17. It can be observed that, even for a long duration $T = t_{\max} - t_{\min}$, satisfactory inversions for capturing the location and convex-hull of the source can be achieved. However, the size of the support becomes

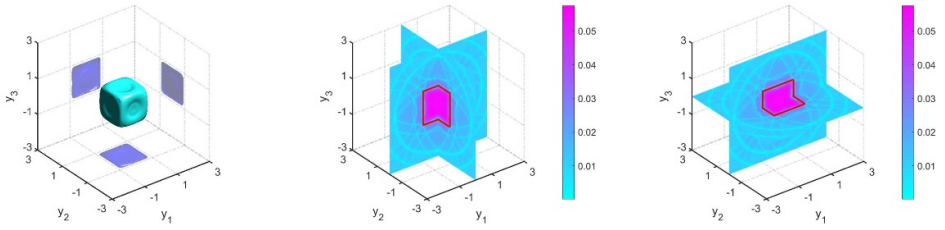

(a) Iso-surface level $= 2.9 \times 10^{-2}$ (b) Slice at $y_1 = 0, y_2 = 0$ (c) Slice at $y_2 = 0, y_3 = 0$

Figure 16. Reconstruction of a cube-shaped support using multi-frequency data from six observation points. The Fourier transform window is $(0, 0.5)$.

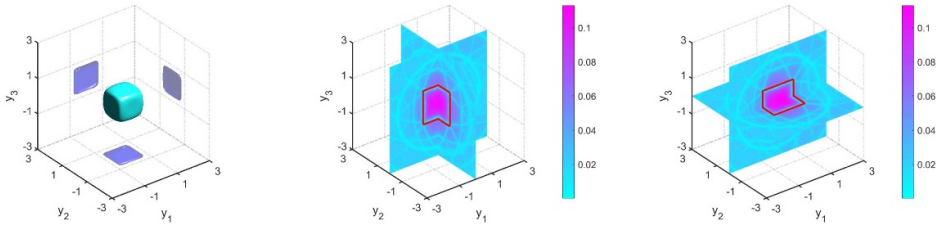

(a) Iso-surface level $= 6 \times 10^{-2}$ (b) Slice at $y_1 = 0, y_2 = 0$ (c) Slice at $y_2 = 0, y_3 = 0$

Figure 17. Reconstruction of a cube-shaped support using multi-frequency data from six observation points. The Fourier transform window is $(0, 1)$.

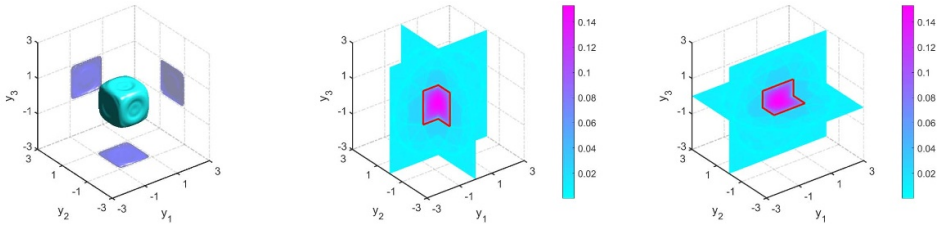

(a) Iso-surface level $= 2.68 \times 10^{-2}$ (b) Slice at $y_1 = 0, y_2 = 0$ (c) Slice at $y_2 = 0, y_3 = 0$

Figure 18. Reconstruction of a cube-shaped support using more multi-frequency data from six observation points. The Fourier transform window is $(0, 1)$. Here we take $N = 400$.

distorted as T increases. The quality on reconstructing the size can be improved by increasing the number of frequencies. The longer the time-dependent source lasts, the more the number of frequencies is needed. Of course the number of observation points affects the resolution of the reconstructions as well. In figure 18, we use more multi-frequency data to improve the quality of reconstruction in figure 17. Here we take $N = 400$ and $K = 20$. It is observed that the cube is nicely restored with more multi-frequency data.

Data availability statement

The data generated and/or analyzed during the current study are not publicly available for legal/ethical reasons but are available from the corresponding author on reasonable request. The data that support the findings of this study are available upon reasonable request from the authors.

Acknowledgments

G Hu is partially supported by the National Natural Science Foundation of China (No. 12071236) and the Fundamental Research Funds for Central Universities in China (No. 63213025).

ORCID iDs

Hongxia Guo https://orcid.org/0000-0001-6361-1982
Guanghui Hu https://orcid.org/0000-0002-8485-9896
Mengjie Zhao https://orcid.org/0000-0003-4946-9646

References

[1] Alves C, Kress R and Serranho P 2009 Iterative and range test methods for an inverse source problem for acoustic waves *Inverse Problems* **25** 055005
[2] Alzaalig A, Hu G, Liu X and Sun J 2020 Fast acoustic source imaging using multi-frequency sparse data *Inverse Problems* **36** 025009
[3] Bao G, Lin J and Triki F 2010 A multi-frequency inverse source problem *J. Differ. Equ.* **249** 3443–65
[4] Bleistein N and Cohen J 1977 Nonuniqueness in the inverse source problem in acoustics and electromagnetics *J. Math. Phys.* **18** 194–201
[5] Chen J, Chen Z and Huang G 2013 Reverse time migration for extended obstacles: acoustic waves *Inverse Problems* **29** 085005
[6] Cheng J, Isakov V and Lu S 2016 Increasing stability in the inverse source problem with many frequencies *J. Differ. Equ.* **260** 4786–804
[7] Colton D and Kress R 2019 *Inverse Acoustic and Electromagnetic Scattering Theory* (Springer)
[8] Elschner J and Hu G 2019 Uniqueness and factorization method for inverse elastic scattering with a single incoming wave *Inverse Problems* **35** 094002
[9] Eller M and Valdivia N 2009 Acoustic source identification using multiple frequency information *Inverse Problems* **25** 115005
[10] Griesmaire R and Schmiedecke C 2017 A factorization method for multifrequency inverse source problem with sparse far-field measurements *SIAM J. Imaging Sci.* **10** 2119–39
[11] Griesmaier R 2011 Multi-frequency orthogonality sampling for inverse obstacle scattering problems *Inverse Problems* **27** 085005
[12] Guo H and Hu G 2023 Inverse wave-number-dependent source problems (arXiv:2305.07459)
[13] Hu G and Li J 2020 Uniqueness to inverse source problems in an inhomogeneous medium with a single far-field pattern *SIAM J. Math. Anal.* **52** 5213–31
[14] Ito K, Jin B and Zou J 2012 A direct sampling method to an inverse medium scattering problem *Inverse Problems* **28** 025003
[15] Ikehata M 1999 Reconstruction of a source domain from the Cauchy data *Inverse Problems* **15** 637–45
[16] Ji X, Liu X and Zhang B 2019 Phaseless inverse source scattering problem: phase retrieval, uniqueness and direct sampling methods *J. Comput. Phys.* X **1** 100003
[17] Kirsch A and Grinberg N 2008 *The Factorization Method for Inverse Problems* (Oxford University Press)

[18] Kusiak S and Sylvester J 2003 The scattering support *Commun. Pure Appl. Math.* **56** 1525–48
[19] Liu X 2017 A novel sampling method for multiple multiscale targets from scattering amplitudes at a fixed frequency *Inverse Problems* **33** 085011
[20] Liu X and Meng S 2021 A multi-frequency sampling method for the inverse source problems with sparse measurements (arXiv:2109.01434)
[21] Liu X, Meng S and Zhang B 2022 Modified sampling method with near field measurements *SIAM J. Appl. Math.* **82** 244–66
[22] Liseno A and Pierri R 2003 Impossibility of recovering a scatterer's shape by the first version of the linear sampling method *AEU—Int. J. Electron. Commun.* **57** 70–73
[23] Liseno A and Pierri R 2004 Shape reconstruction by the spectral data of the far-field operator: analysis and performances *IEEE Trans. Antennas Propag.* **52** 899–903
[24] Liseno A and Pierri R 2002 Imaging perfectly conducting objects as support of induced currents: Kirchhoff approximation and frequency diversity *J. Opt. Soc. Am.* A **19** 1308–18
[25] Ma G and Hu G 2022 Factorization method with one plane wave: from model-driven and data-driven perspectives *Inverse Problems* **38** 015003
[26] Nakamura G and Potthast R 2015 *Inverse Modeling: An Introduction to the Theory and Methods of Inverse Problems and Data Assimilation* (IOP Publishing)
[27] Potthast R 2001 *Point-Sources and Multipoles in Inverse Scattering Theory* (*Chapman & Hall/CRC Research Notes in Mathematics* vol 427) (CRC Press)
[28] Potthast R 2010 A study on orthogonality sampling *Inverse Problems* **26** 074015
[29] Sylvester J and Kelly J 2005 A scattering support for broadband sparse far field measurements *Inverse Problems* **21** 759–71
[30] Zhang D and Guo Y 2015 Fourier method for solving the multi-frequency inverse source problem for the Helmholtz equation *Inverse Problems* **31** 035007